ADVANCED ENGINEERING MATERIALS
www.aem-journal.com

Laser Metal Deposited Ti4822 Hollow Pipe: Experimental and Computational Modelling Study

Sadiq A. Raji, Monnamme Tlotleng, Samuel Skhosane, Lehlogonolo R. Kanyane, Abimbola P. I. Popoola, and Sisa L. Pityana*

Generally, manufacturing valuable parts from General Electric's titanium aluminide (Ti-48Al-2Cr-2Nb; Ti4822) is extremely difficult. The difficulty is due to the alloy's poor room temperature castable and machining properties. To achieve functional parts from Ti4822 via cast and selective laser melting, built parts are hot isostatically pressed. Unfortunately, direct energy deposited Ti4822 parts are yet to be reported in open literature and hence this article wherein a 100 mm long pipe is laser metal deposited and investigated for use as a heat exchanger. Before printing, the theoretical model is used to predict geometric defects (tapering) and heat distribution. The results conclude tapering at around 30 mm and rapid increase in heat inputs (HIs). The microstructural analyses corroborated this observation, particularly the fracture analyses which indicated internal cracking, impurities and pores at moderate HI, and isotropic microstructure with elongation formed dimple grains at high HI position. Fracture is said to be transgranular, cleavage-like, and ductile-brittle overall. Nanoindentation results conclude that the pipe would withstand high stress due to high toughness. Pipe inner surface roughness is 5.190 µm, indicating acceptable pressure drops and therefore usable as a heat exchanger.

1. Introduction

Industrialization of titanium aluminide (Ti–Al) alloys has been an ongoing effort given their difficulty in manufacturing and postprocessing. Ti–Al alloys have desired properties for applications ranging from room-to-high temperature application. In addition, they are light in weight and when used as aeroplane frames will aid in payload reduction, thereby leading to fuel cost savings. This is their major need for commercialization. Moreover, their ability to withstand high-temperature creep conditions with minimum to zero dislocations had opened scope for material requirements necessary for extreme high-temperature application beyond conventional operations. The uptake by industries is hampered by their heat sensitivity that during processing, the printing part(s) would lift off from the built platform, and the overall part built will have defects and faults such as pores, cracks, chemical imbalance, and inhomogeneity. The built is highly anisotropic with dislocations forming along the grain boundaries. These faults compromise their performance. Nonetheless, efforts from researchers on the quest to cast or 3D print crack-free Ti–Al artifacts are still ongoing. To date, positive results are being reported on the progress of alloy developments, processing, postprocessing, and machine re-engineering.[1]

Commercial Ti–Al alloys are summarized by[2] Nochovnaya et al. but there have since been several more alloys that were developed in-line with parts' performance. Recent studies on alloys have a particular focus on obtaining an alloy with balanced chemistry which will have good room temperature (RT) ductility and flowability given that more advance manufacturing facilities are now available. In processing, the dilemma of achieving densely uncracked parts and the efforts on hot isostatic pressing of cast Ti–Al have yielded positive

S. A. Raji, L. R. Kanyane, A. P. I. Popoola, S. L. Pityana
Department of Chemical
Metallurgical and Materials Engineering
Tshwane University of Technology
Staatsartillerie Road, Pretoria West, Pretoria P.M.B. X680, Gauteng Province, South Africa

The ORCID identification number(s) for the author(s) of this article can be found under https://doi.org/10.1002/adem.202500737.

[Correction added on 18 November 2025, after first online publication: the third and sixth authors' affiliations have been updated in this version.]

DOI: 10.1002/adem.202500737

M. Tlotleng
Material Science Innovation and Modelling Research Group
Mahikeng Campus
North-West University
Mmabatho, Mahikeng, North West Province 2790, South Africa
E-mail: daopase@gmail.com

M. Tlotleng
Instrument Research and Development Group
Measurement and Control Division
Mintek, 200 Malibongwe Drive, Praegville, Randburg, Johannesburg, Gauteng Province 2194, South Africa

S. Skhosane, S. L. Pityana
Laser Enabled Manufacturing (LEM) Research Group
Photonics Centre
Council for Scientific & Industrial Research (CSIR)
Pretoria 0184, South Africa

outcomes, but the process is cost intensive. Using either selective laser melting or electron beam melting (EBM), which are categorized as powder bed systems (PBSs), researchers have suggested that a crack-free artifact can be fabricated, but this has not been achieved to date. PBSs are smart 3D printing machines with the capability of being able to control and monitor heat inputs during manufacturing. It was not until recently (2017/8) that Arcam-General Electric Additive Group was able to demonstrate a functional EBM machinery, named Arcam EBM Spectral H, which is dedicated to 3D printing difficult intermetallic alloys such as Ti–Al alloys, wherein a produced part is fully dense and has required industrial useful properties.[1] On the other hand, engineers using laser metal deposition (LMD) systems have argued that by re-engineering how the laser beam and powder stream interact, it would be possible to fabricate the intermetallic powders and produce a crack-free artifact. To date, there are yet credible results to be reported in open literature on this assertion.

In the quest to continue using LMD process and to achieve a crack-free built, researchers have proposed that in addition to a defocused laser beam, the base plates (also known as substrates) should be preheated. The reasoning is that the thermal mismatch between the melt-pool powder stream and the base plate will be averted. It is understood that these mismatches lead to temperature gradients that are responsible for the thermal cracking during the deposition of crack-sensitive alloys such as Ti–Als. This hypothesis has also not brought forward convincing results, but suggestions of printing on a heated bed or carefully controlled environment are yielding positive results.[1] In contributing to the existing research in this field of manufacturing titanium aluminide components, this article reports the results of a 15 mm-diameter hollow pipe that was laser metal deposited from a Ti-48Al-2Cr-2Nb (Ti4822), GE Ti–Al powder. The results presented in this article capture both the theoretical (using COMSOL software) and experimental outcomes of the printed hollow pipe. The printed pipe was 100 mm in length with internal and outer diameters of 15 and 19 mm and wall thickness of 4 mm. The pipe was studied for microstructure, surface roughness, fracture, microhardness, and nanoindentation.

2. Modelling

2.1. Governing Equations

In this study, a 3D model of a cylindrical hollow pipe was computed using COMSOL Multiphysics 5.5 to simulate the effects of preheat at 800 °C during LMD processing of a Ti4822 alloy. Ti–Al alloys are usually processed in a well temperature-controlled environment, and therefore, this simulation helped in understanding the stress evolution and thermal behavior of the hollow pipe during LMD processing. The energy density of the laser beam was computed based on Equation (1)[3]

$$E = \frac{P}{vd} \tag{1}$$

where E is the energy density of the laser beam in J mm^{-2}, P is the laser power in Watts (W), d is a diameter of the laser spot size in mm, and v is the laser scanning speed in mm s^{-1}.

2.2. Governing Equations

Based on the principle of heat transfer (in solids), the 3D transient temperature field heat source during LMD processing of a Ti4822 was determined by the Fourier heat differential equation (Equation (2) and (3))

$$\rho C_{\mathrm{p}} \frac{dT}{dt} + \rho C_{\mathrm{p}} u \cdot \nabla T + \nabla \cdot q = Q + Q_{\mathrm{ted}} \tag{2}$$

$$q = -k \nabla T \tag{3}$$

where C_{p} is the specific heat in J kg^{-1} K^{-1}, ρ is the density in kg m^{-3}, T is the temperature in Celsius degrees (°C), t is time in seconds (s), Q is the internal heat source intensity in J mm^{-2}, and k is the coefficient of thermal conductivity in W/(m.K), while the C_{p} and k change with temperatures.

Likewise, the structural deformation mechanics were predicted based on Equation (4). This was used to determine the behavior of the material to deformation as a result of heat accumulation during laser processing or fabrication

$$\rho \frac{\partial^2 u}{\partial t^2} = \nabla \cdot S + F_{\mathrm{v}} \tag{4}$$

where ρ is the density in kg m^{-3}, u is a vector quantity, S is the translational transformer, t is time and F is the linear transformer.

2.3. Material Properties

Materials' thermophysical properties have tremendous effects on the temperature regime that precisely controls the size and shape of components produced through the laser fabrication process. It is essential to state that the thermal properties of materials are temperature dependent; thus, the average values of these various properties are used during the simulation study. The thermophysical properties of Ti4822 alloy are stated in **Table 1**.

2.4. Model Heat Source

The LMD process is a moving heat source along the axes being specified. To study the temperature fields in LMD processing, the finite element model is needed to determine the heat source

Table 1. Thermophysical properties of Ti4822 alloy.

Description	Values
Coefficient of thermal expansion	8.6×10^{-6} K^{-1}[25]
Density of material (liquidus)	3780 kg m^{-3}[25]
Density of material (solidus)	3900 kg m^{-3}[25]
Heat capacity of material	610 J/(kg·K)[25]
Thermal conductivity material	20 W/(m·K)[25]
Young's modulus	1.72×10^{11} Pa[3]
Poisson ratio	0.22[3]
Liquidus temperature	1807 K[25]
Solidus temperature	1719 K[25]
Thermal transmittance	15 W/(m^2 K)[3]

model based on the material thermophysical property and meshing situation. The laser heat source which is a Gaussian distribution is presented in Equation (5)

$$f = \frac{2 * \text{Power}}{\pi r^2} e^{\left(-2\frac{(x^2+y^2)}{r^2}\right)} \quad (5)$$

where $x = R * \cos\theta$ and $y = R * \sin\theta$, f is the heat flux in J mm^{-2}, r is the radius of the laser beam in mm, R is the radius of the cylindrical pipe, and Power is the power of the laser beam in Watts, while x and y are the variables indicating the distance from the center of the laser beam. The heat flux is applied based on Equation (5) which is a Gaussian profile as shown in **Figure 1**. The laser beam movement is according to the coordinate system defined along the axes.

The model heat source is useful in assessing the temperature fields of laser material processing employing the finite element analysis (FEA) method. This would give high accuracy of results from the model especially for cases where the laser beam heat source. Therefore, simulation of laser processing through Gaussian heat source could be manipulated to move based on a predefined sequence of finite element modelling which also provides consistent heat flux density at distinct movement and positions.[4,5]

2.5. Geometry and Meshing

In as much as LMD is a technique characterized by drastic changes in temperature and a very high-temperature gradient, accurate thermal modeling is essential to capture the transient heat transfer behavior. The meshing of the laser scanning regions and surroundings should be accurately subdivided, while other regions could be approximated. The model finite element mesh is displayed in **Figure 2**. The COMSOL Multiphysics applies the arbitrary Lagrangian–Eulerian formulation method for the moving mesh with a hyperelastic smoothing method.[6] The direct PARDISO solver resolution is adopted with accompanied solvers. A free tetrahedron mesh type of 129,880 elements

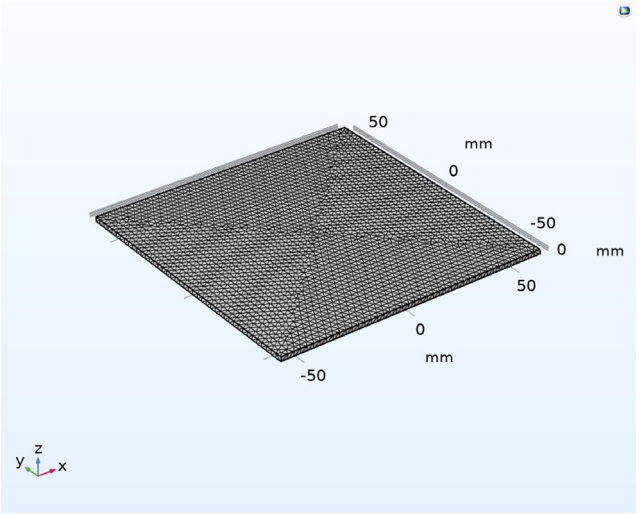

Figure 2. Model tetrahedral meshing.

with a maximum and minimum size of 0.0066 and 0.0048 µm, with a curvature factor of 0.4, is used. The absolute tolerance is 10^{-3}, and the relative tolerance is 10^{-2}. The simulation was performed on four cores on a 16 GB RAM computer with the Windows 10 operating system, taking a total time of 5 h 29 min to complete up to a height over 100 mm. Moreover, the effects of the moving mesh on the size of the molten pool are minimal.[7] Also, the error on the energy conservation during modeling remains less than 10% for the deposition.

2.6. Model Assumptions

To simplify the model and keep it close to real-life scenarios, some assumptions were made to make the simulation less cumbersome and complicated. These assumptions are as follows: 1) The material is isotropic. 2) There is no heat loss by conduction. 3) Only the top surface (boundary) of the substrate is not

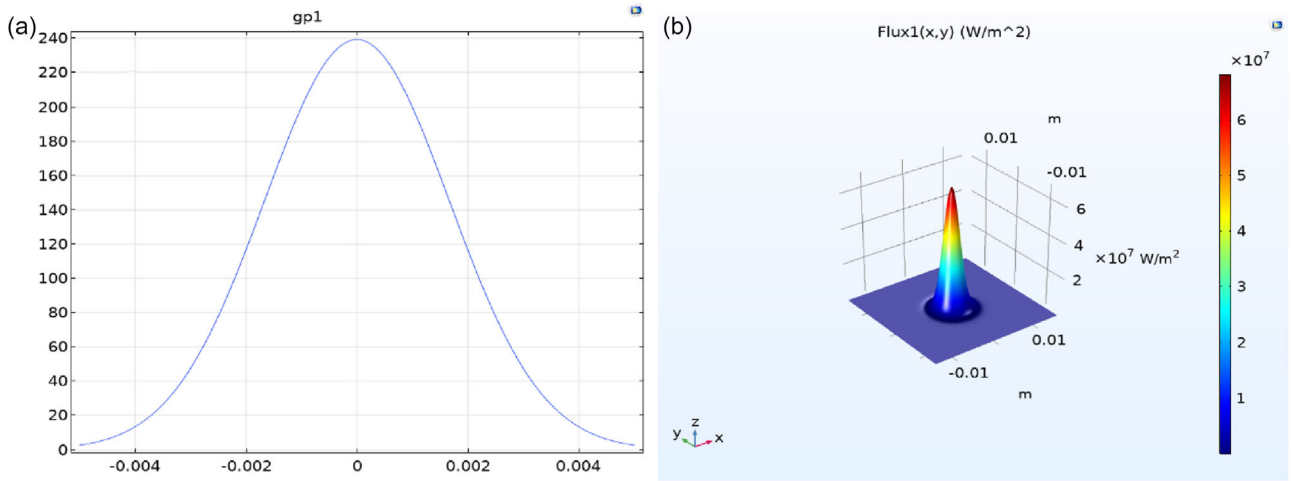

Figure 1. Showing the a) analytical graph of the Gaussian profile and b) Gaussian pulse.

thermally insulated. 4) Material vaporization was neglected. 5) The material is linearly elastic. 6) The flow function of the melt pool is neglected.

3. Experimental Section

3.1. Materials

A commercially available Ti4822 powder was used as feedstock. The power was supplied by WEARTECH (Pty) Ltd., Johannesburg, South Africa, and was spherical with particle size distribution that ranged between 45 and 90 μm and had a chemical composition as shown in **Figure 3**.

3.2. Methods

3.2.1. Laser Metal Deposition

The LMD setup used in this work was available at the laboratories of the CSIR, South Africa. This facility is called Eskom laser. The setup has a 3 kW maximum power output IPG fiber laser as an energy source which together with the coaxial head are attached to the Kuka robot arm. The robot arm controlled the axial motions during deposition and deposited the powder, which was contained in a GTV powder feeder, into a melt pool that was generated on the Ti-64Al-4V substrate with dimensions of $70 \times 70 \times 7\ mm^{-3}$. The schematic representation of the process setup and the printed sample is shown in **Figure 4**. Before deposition, the base plate was sandblasted (to circumvent laser beam reflections) and cleaned with acetone. During processing, the substrate was placed on top a heating stage that was set to the temperature of 800 °C.

The LMD process parameters that were used are reported in **Table 2**.

After manufacturing the pipe, the chemical composition of the as-built pipe was determined using the scanning electron microscopy (SEM)-energy-dispersive X-ray analysis (EDS) and the

Table 2. LMD optimized process parameters used.

Laser power	Laser scan speed	Powder feed rate	Temperature	Carrier gas	Shielding gas
1000 W	1.5 m min^{-1}	1.2 rpm	800 °C	1.8 L min^{-1}	15 L min^{-1}

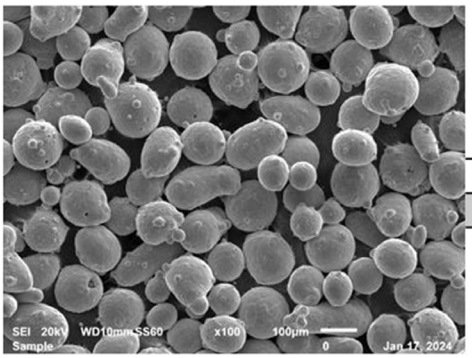

Chemical composition

Element	Ti	Al	Cr	Nb
Atomic (%)	50.29	47.2	1.13	1.38

Figure 3. Morphology and chemical composition of the as-received Ti4822 powder.

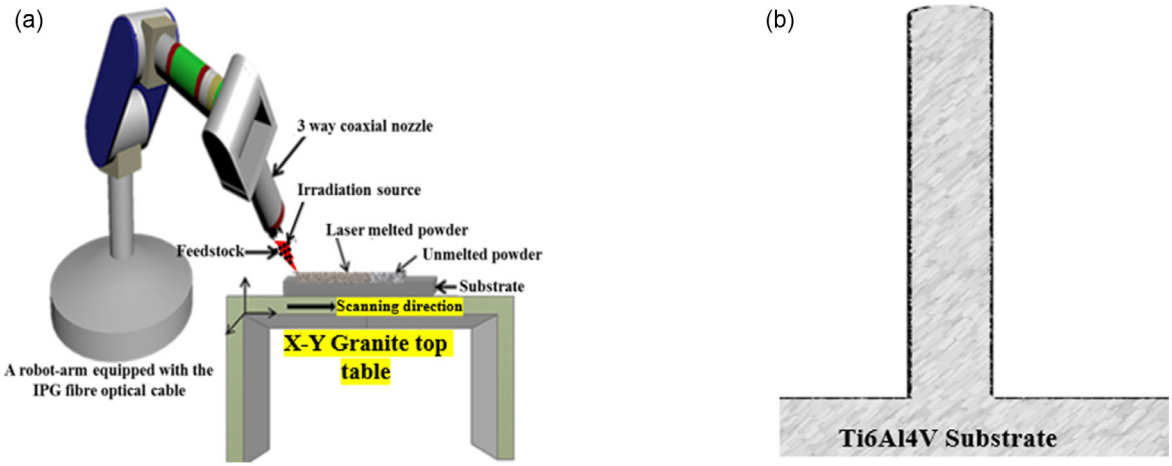

Figure 4. Schematic diagram of the a) process setup and b) produced sample.

Table 3. Chemical composition of the built pipe.

Built pipe	Ti	Al	Cr	Nb
Contour surface	41	56	2	1
z-direction	40	57	2	1
Average	40.5	56.5	2	1

results are reported in **Table 3**, indicating that the produced pipe was pure gamma due to the aluminum % content reported.

3.2.2. Sample Preparation and Characterization

After sample manufacturing, the built pipe was taken for (inner and outer) surface roughness measurement using Elcometer 7061 MarSurf PS1 Surface Roughness Tester. After surface roughness measurements, four specimens (2 curve contours and 2 flat sections along z-built direction) were extracted from the pipe and taken for metallographic preparations. One set of samples was mounted and polished to a 0.04 micron (OP-S suspension) surface finish using a Struers TegrsForce-5 auto/manual polisher. The samples were etched for about 30 s by immersing in a Kroll's reagent. Olympus BX51M mounted with the SC30 camera was used for the microstructural and defect observations. The samples were analyzed for chemical composition using Joel, JSM-6010Plus/LAM SEM that was equipped with EDS. Microhardness measurements were conducted with Zwick/Roell (ZHVμ) Vickers hardness machine. The loading force of 500 gf with a dwelling time of 10 s was used. Nanoindentation hardness tester (Anton-Paar TTX-NHT3) was used to investigate the nanomechanical properties of the direct energy deposited (DED) fabricated cylindrical pipe. The nanoindentation tests carried out used a maximum load of 200 mN for a total time of 60 s per indents with the loading, holding, and unloading time of 20 s each. The indentation results gave a representation of the samples' mechanical properties (Young's modulus, stiffness, and indentation hardness). The Oliver and Pharr method was adopted for analyzing the load displacement curve.[8] The other set was mounted and not polished and was studied from fracture analysis.

4. Results

4.1. Model Results

Figure 5 illustrates the temperature profiles indicating the maximum temperatures, minimum temperatures, average temperatures, and the difference between the maximum and minimum temperatures of the simulated LMD process at 800 °C preheat.

There is an acute increase in temperature and rapid cooling, seen from Figure 5, as the laser beam moves along the x–y direction. The maximum and average temperature and the difference between the maximum and minimum temperature increase further with the increase in time and additional layers with the peak temperature reaching about 6000 °C. This shows that the heat is retained due to the continuous heating and maintaining the ambient (minimum) temperature at 800 °C. Hence, temperatures of preceding layers continually increase with the addition of more layers. Before 20 s, the path showing a rise in temperature with time conforms with the deposition period of the layer. Also, the path indicative of temperature reduction with time conforms with the idle time when the laser beam moves to successive deposition of layers. However, after 20 s, the temperature increases steadily without showing any form of reduction in temperature with time. Consequently, thermal cycles and peak temperatures experienced by the respective layer of deposits affect the resultant dimensional accuracy and mechanical properties of the component.[9,10]

Figure 6a–f shows the surface temperature profile of the laser beam during deposition at steady state. The preheating temperature tends to demonstrate high influence in the temperature distribution which could easily be altered by other processing parameters like the scanning speed, laser power, and beam diameter (though they were constant). Also, this shows the high energy intensity within the deposited part and acute temperature

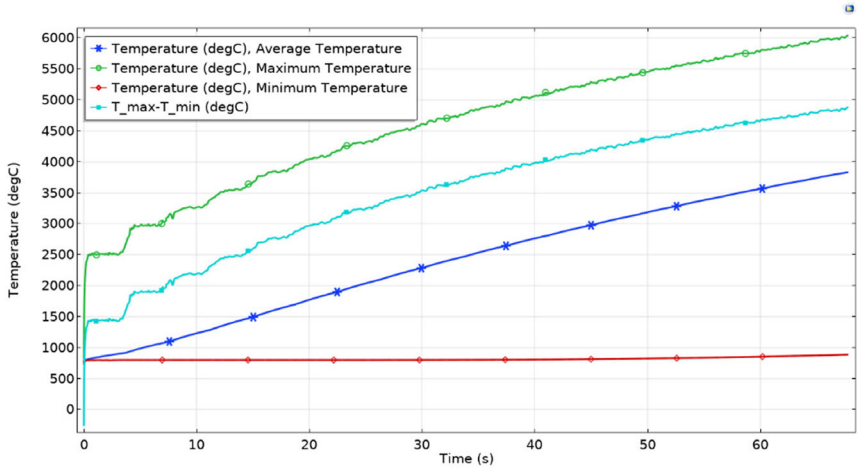

Figure 5. Probe plots showing the maximum, minimum, and average temperatures and the difference between the maximum and minimum temperatures during the laser heating.

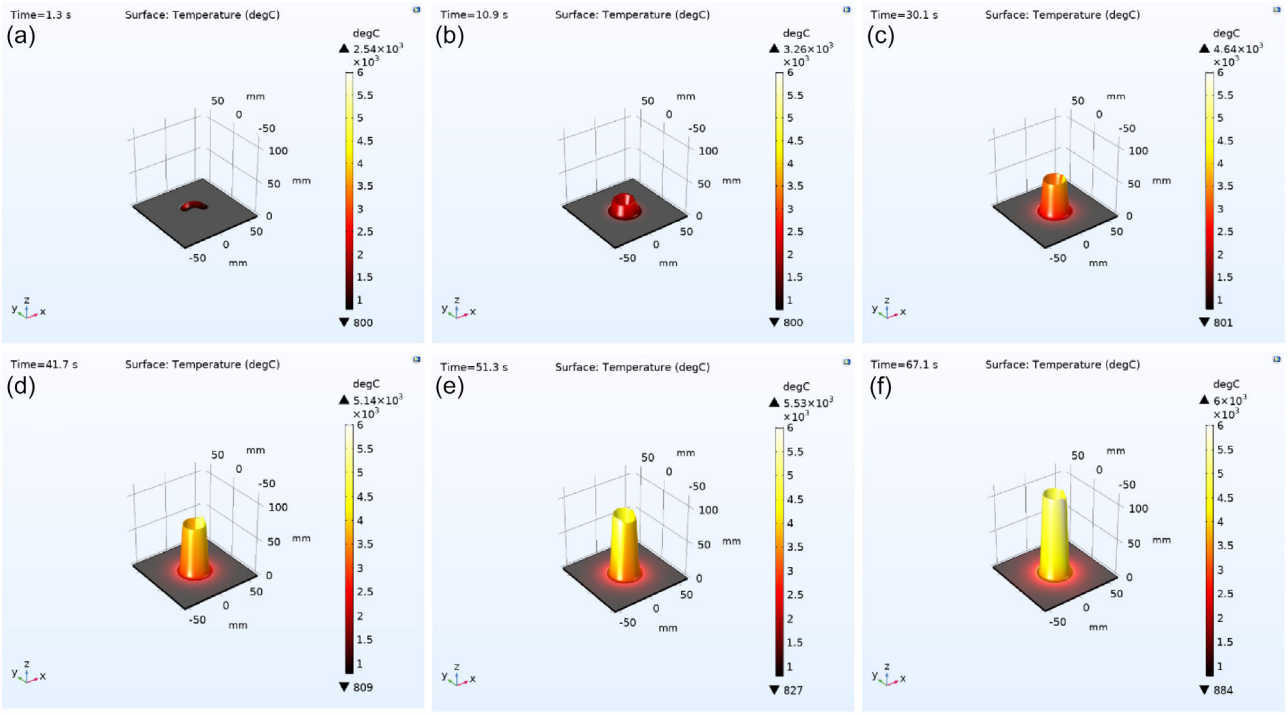

Figure 6. Temperature distribution profile of the cylindrical pipe in 3D at time a) 1.3 s, b) 10.9 s, c) 30.1 s, d) 41.7 s, e) 51.3 s, and f) 67.1 s.

gradient at small intervals of the laser beam. It could be deduced from the results in Figure 6 that a higher temperature and a larger melt pool would lead to a higher material buildup.[11] This effect can be noticed between the bottom portion and toward the middle section of the cylindrical hollow pipe. There seems to be an acute increase in the temperature as the pipe height range was about 40–50 mm. The rapid temperature increase was accompanied by rapid cooling or solidification conditions. Typically, this condition, known as thermal stress, leads to delamination and cracking of the built sample. The stress profile of the built pipe is reported in **Figure 7**.

From Figure 7, it can only be seen that the sample experienced tapering and surface tearing. The effect of surface tears and tapering is a result of a molten pool becoming more liquid and uncontrollable at the constant powder feedrate. Because of the constant powder feedrate, at a point, the temperature will build up and lead to over melting. This will result in wall thinness (tapering) and misalignment, thereby powder depositing on the sides leading to surface tearing. To elucidate this condition, the Von Mises stresses for the simulated LMD-processed Ti4822 alloy, at continuous preheating at 800 °C, are shown in **Figure 8**. The beam position is indicated by a, b, c, and d positions on the pipe.

Figure 8 shows that stress accumulation will increase with the duration of the laser beam during 3D printing. This means that the stress will be lowest at position "a" (Figure 8a), will increase between positions "c and d" (Figure 8c,d respectively), and will be highest at position "d" (Figure 8d). The maximum Von Mises stress of 2.9 GPa was identified at the position with the highest temperature (position "d"). Thus, it could be deduced that the thermal gradient influences the stress levels at specific time and positions. This could be corroborated by the report of[3] Balichakra et al. which predicted that the Von Mises stress would be maximum at the spot with the maximum temperature value noted throughout the process of irradiation. It is understandable that the stress does not surpass the material yield strength (YS) to minimize crack initiation and propagation. Figure 7 shows the stress contour of the cylindrical pipe in 3D, while Figure 8a–f shows the stress levels at specific times. It could also be noticed that the stress in-built increases drastically as the height reaches between 40 and 50 mm. These stress profiles indicate the

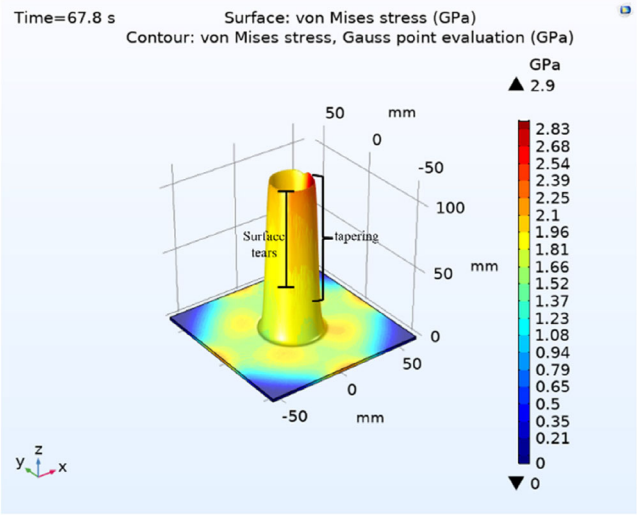

Figure 7. Stress profile of the 100 mm cylindrical hollow pipe.

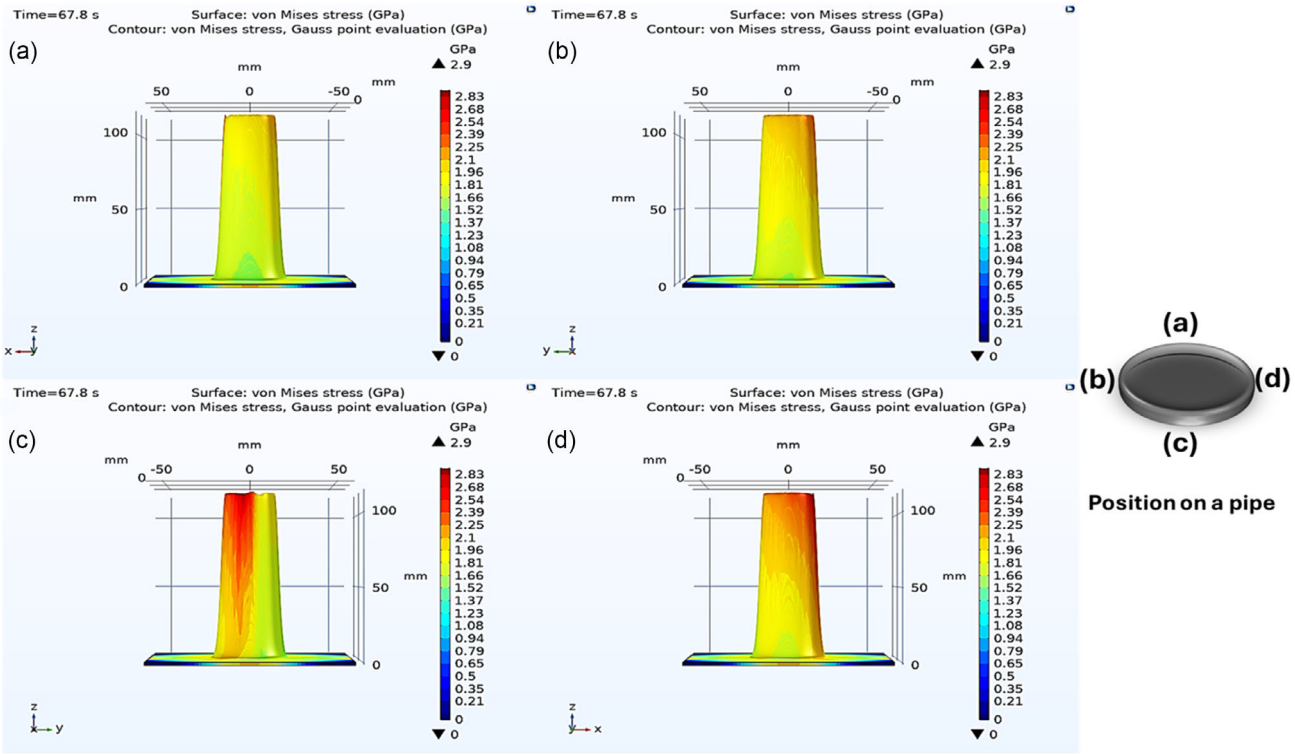

Figure 8. Showing the stress contours on the 100 mm cylindrical pipe along a) positive yz direction, b) negative yz direction, c) positive xz direction, and d) negative xz direction.

possible positions where the built pipe might fracture (stress fracture) during load. The model was used predict the stresses along the contour of the pipe during printing, and the corresponding SEM image analyses are reported in **Figure 9**.

From Figure 9a–f report a lamellar grained microstructure with identified defects. Along the pipe growing direction building (flat surface (Figure 9d–f)), there are interlocked lamellar grains (Figure 9e) and stress pile-ups (Figure 9f). A lamellar grained microstructures that are interlocked at the boundaries are said to be tolerant to fracture. The curved image analyses (contour building directions), as reported in Figure 9a–c, indicate cracking which will serve as initiation sites for failure in the built pipe. What these images convey is that the pipe will definitely fail along the contour.

4.2. Surface Roughness and Microstructure of the Outer Surface of the Pipe

Surface roughness and material defects have a strong influence on the mechanical performance of additively manufactured (AM) parts. Surface roughness and the anisotropic behavior of AM parts affect the mechanical behavior of the build, and moreover, since manufacturing is achieved in a layer-by-layer fashion, it is reported that the microstructure, at the boundaries, is completely different from that of the internal surface. This led to different mechanical behaviors of the as-built AM parts. **Figure 10** depicts the pipe surface roughness in the as-built state and corresponding microstructures.

From the measurements reported in Table 3, it was noticed that the bottom (position "f" = 16.5 mm) and top (position "a" = 100 mm) ends of the pipe had the highest roughness. This surface roughness is obviously due to the resulting sputter and the accumulation and agglomeration of unmelted and fine powder onto the substrate and the built part as is with DED processing. The pipe had a similar roughness that ranged between 3.22 and 3.39 μm in the middle (position "c" = 33 mm, position "e" = 66 mm, and position "d" = 49,5 mm), and the lowest roughness was reported for the height built of 82.5 mm (position "b"). The average surface roughness of the built pipe is 3.49 μm as summarized in Table 3. The range for DED powder-blown AM machines is recorded at about 4–200 μm.[12] Nunez III et al. reported surface roughness of 8.94–38.77 μm and 3.21–42.91 μm, for laser engineered net-shaping (LENS) fabricated 316L and IN718, respectively. The average roughness reported in this study is below the overall reported range for DED machines, indicating that the process parameters used (energy density and powder feed rate) were highly optimized to produce a high-quality, fully dense, and least rough part.

The other Ra values were very close to each other. Moreover, the corresponding microstructures were investigated using SEM which revealed that the pipe on the surface has particles that can be said to be oxides. From top to bottom, the microstructure is similar showing smooth lamellar-grained structure (30–25 mm). From 20 mm, the formed lamellar grains are seemingly rough, and microstructures from 15 to 10 mm are characterized by thick or coarse lamellar structures that seem to be precipitating out of

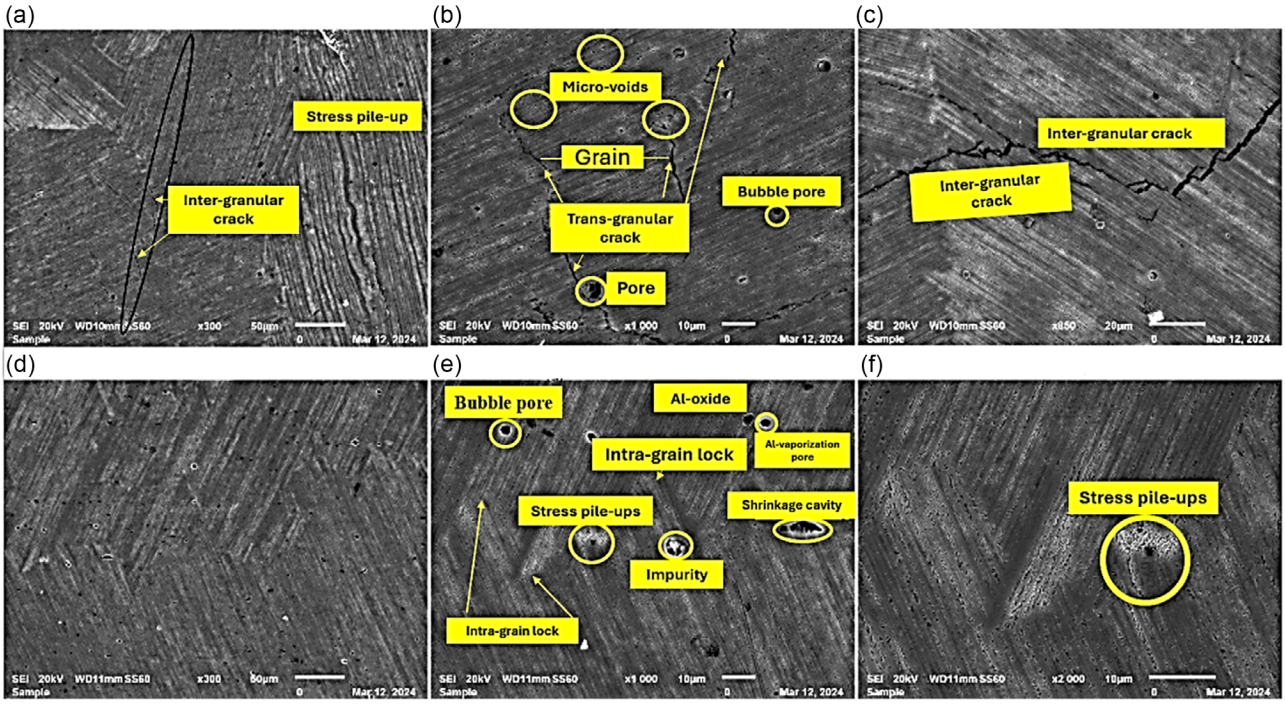

Figure 9. Microstructure showing defects.

the matrix and are different from the earlier observed grain structure. The built microstructure, 5 mm from the substrate, is a grained lamellar microstructure with some grains being smooth (left side of the image) and other rough (right-side of the image). The rough grain is a sign of dislocations that resulted during printing. All the observed features are the reason for the overall rough surface achieved and the known fact that powder-blown manufacturing systems generally have difficulty in achieving a smooth surface. The average surface roughness of the inside of the pipe was measured at 5.190 µm wherein the bottom end and top end roughness were 6.031 and 4.348 µm, respectively.

Microstructures of the outer surface of the hollow pipe are summarized in **Figure 11**. The microstructures are along the build direction and the contour of the pipe. These microstructures show a smooth, lamellar structure along the built direction (z-direction). Figure 11a shows a lamellar grain structure which is smooth and well-aligned, indicating that there are no dislocation pile-ups. Unfortunately, the same cannot be said about the lamellar grain structure reported in Figure 11b. A highly resolved image of these grains, **Figure 12**, shows dislocation pile in the adjoining grains. From this figure, it is clear that the pile-ups are present in the aluminum lean phase (α_2 phase-white color), while aluminum-rich grains (γ phase-dark color) are void of dislocations. These results overall suggest that the pipe would fracture along the contour direction (crack initiation sites) as opposed to along the built direction.

4.3. Fracture Analysis

There is an understanding that there is a strong correlation between the microstructure and fracture toughness for gamma titanium aluminides at RT.[13,14] **Figure 13** shows the fractography micrographs of the built pipe in the as-built state (RT).

Different features are identified per zone; for instance, in Figure 13a, the micrograph shows the evidence of intergranular cracking and pores. This type of fracture results from a combination of impurities, pores, and high stresses within the material causing embrittlement; such defects permit the cracking to propagate along the grain boundaries. The presence of voids and impurities along the grain boundaries causes a stress raiser which then requires less stress to propagate the crack. During laser welding or laser additive manufacturing, pores arise from entrapped gas due to poor shielding and insufficient heat input. Insufficient heating also led to the lack of fusion or partial particle melting which can cause defects in the built part. Thus, applying any load on a built with voids may result in the coalescence of voids forming cracks along the grain boundary. Figure 13c,d micrographs show no pores/impurities but instead intergranular and transgranular cracking which is an indication of ductile-to-brittle transition. However, Figure 13d shows dimple-like and elongated grains which are the indication of ductile failure mode. The production of ductile structures in welding fabrication is associated with the tempering of the microstructure. High heat inputs yield slow solidification allowing the softening and removal of entrapped gas which is the effect of an increase in laser interaction time during laser printing. Figure 13b sample shows cleavage intergranular fracture with lamellar subgrain and grain elongation in the build direction (+z-direction). These microstructural features induce fracture tolerance in the built sample.[15] There are no pores or impurities that are observed in Figure 13b, and therefore, it can be said that this part of the sample will fail in ductile mode leading to an overall

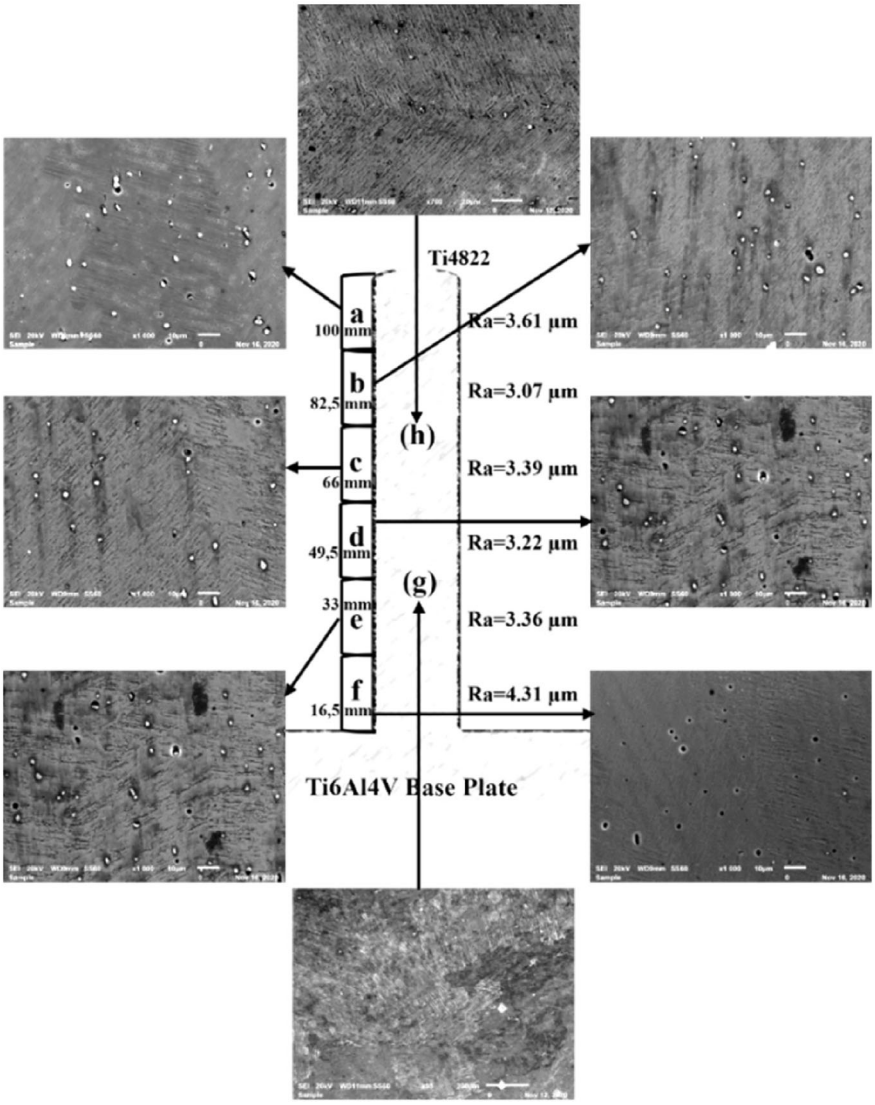

Figure 10. Microstructures and surface roughness (Ra values).

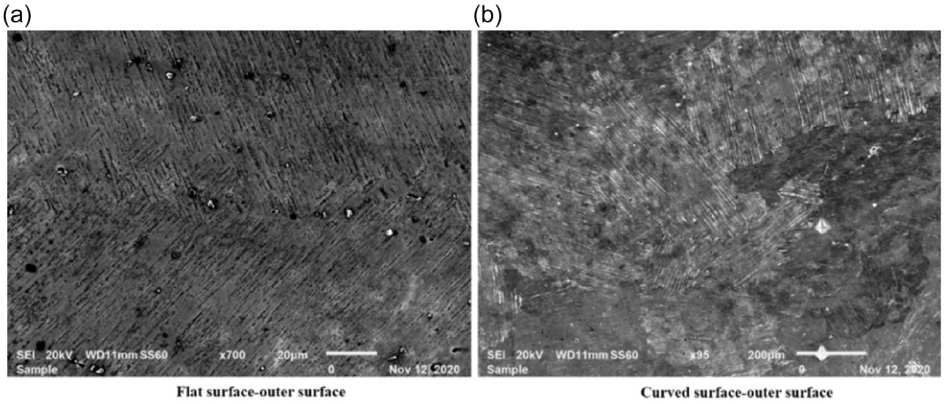

Figure 11. Microstructure of the outer surface of the built hollow pipe.

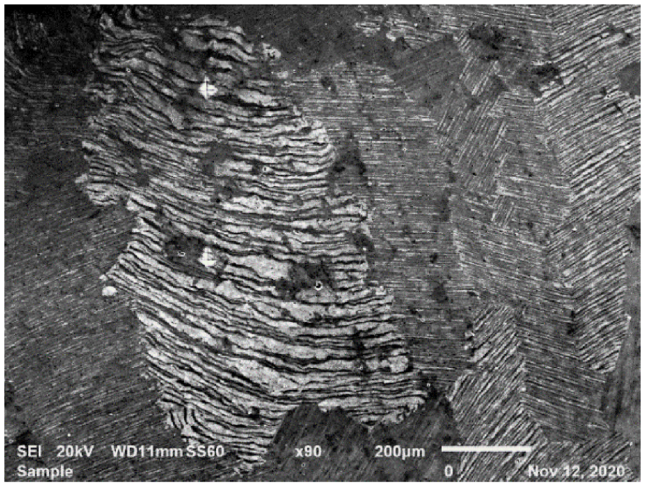

Figure 12. Resolved grains of the contour.

observation that indicates that the built pipe failed due to a combination of these effects and such failure can be summarized as transgranular cleavage-like failure. A similar observation is reported by[13] Kim and[14] Gnanamoorthy et al.

4.4. Microhardness

Indents, also known as impressions, from hardness measuring techniques can be used in predicting how materials would behave by envisaging material properties such as hardness, elastic modulus, and fracture toughness. Fracture toughness depends on the number of cracks generated around Vickers impression. These cracks are either radial or nonradial. The radial cracks that remain intact to the indent are called radial-median crack, and those that detach from the indent are called Palmqvist cracks. To distinguish the fracture mode or the type of a fracture that might occur in print material, the post hardness measurement indent (the Vickers impression) morphologies are analyzed. Typically, fractures occur at the edge of the residential indentation impression, and the morphology can be used to infer or descent the modes of fracture: brittle fracture, cleavage fracture, or transgranular fracture.[16] The indents of the pipe, on the curve (around contour) and flat (along pipe height build), are shown in **Figure 14**.

Two loads were used to investigate to the failure of the sample. It can be seen that at positions a–b, for both 1000 and 2000 gf, the sample shows no signs of deformation or failure, and at position c, the sample started to deform until it permanently deformed at 1000 gf (position d) and fractured under 2000 gf (position "d").

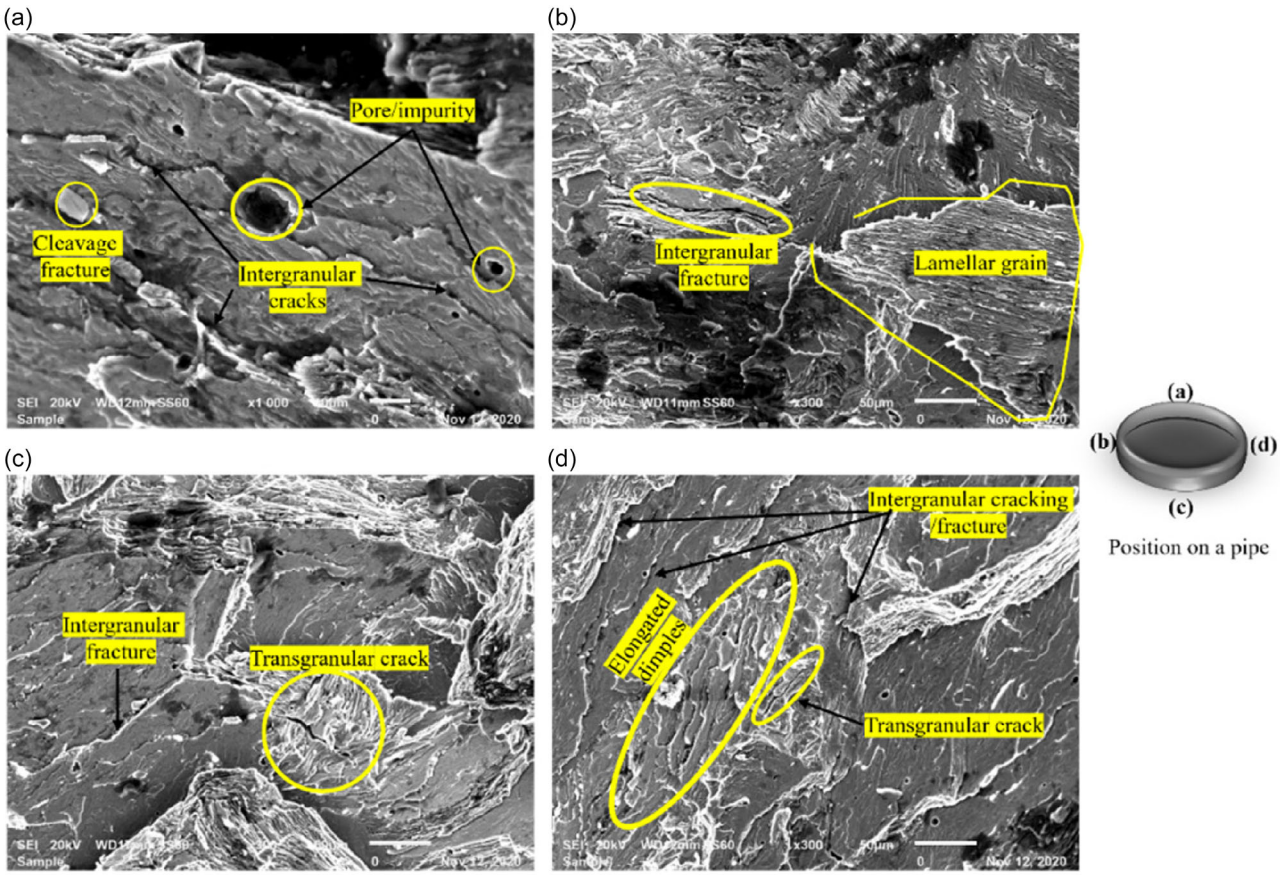

Figure 13. Fracture SEM images of the built pipe over the pipe contour.

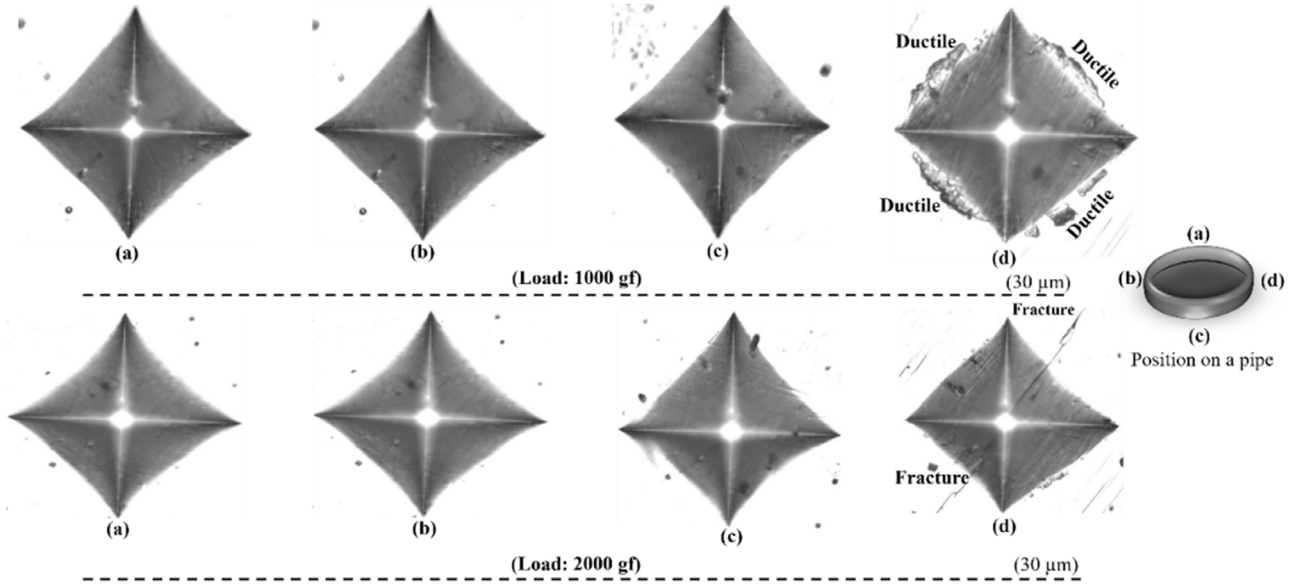

Figure 14. Morphology of Vickers impressions.

What this indicate is that during load, the sample will go through plasticity deformation and then permanently deform until it fractures. The sample has Palmqvist cracks, and the fracture mode can be summarized as ductile to brittleness as shown intuitively in **Figure 15**.

4.5. Nanomechanical Properties

The results reported in this article are of a 100 mm hollow pipe tube that was 3D printed from GE alloy using the LMD process, while the Ti-6Al-4V substrate was placed on a heating platform that was continuously heated and held at 800 °C during deposition. Process development of 3D printing crack-free GE alloy on a Ti-6Al-4V alloy substrate using the same setup, process parameters, and conditions was reported earlier by the same authors.[17] Their study summarized that a crack-free cube was manufactured by depositing spherical GE Ti4822 alloy powder using laser direct metal deposition technique. Tensile specimens were wire cut and tested for tensile properties. Three kinds of specimen were tested: the as-built and those that were heat treated in an argon-rich environment at 1200 and 1400 °C and oven cooled. The results showed that the as-built samples had high ultimate tensile strength (UTS) of (440.68 MPa) and very poor elongation (0.11%), while samples that were heat treated at 1200 and 1400 °C had UTS of 382.95 and 297.60 MPa, respectively, as summarized in **Table 4**.

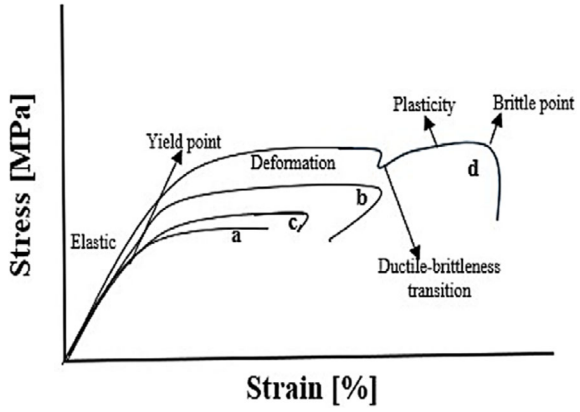

Figure 15. Extrapolated tensile behavior of the pipe along the curve surface at varied positions (a–d).

Figure 16 shows stress–strain curve (a) and load versus displacement curve (b). From Figure 16a, the curve material (blue drawing) failed in brittle mode at about 564 MPa UTS, and it exhibits a high YS of 360 MPa, high stiffness, and less ductility, while the flat surface (straight section) failed at low UTS. However, it poses good ductility as summarized in **Table 5**. Nanoindentation results presented in Figure 16b shows load versus displacement graph where the curve material (blue drawing) shows high modulus of elasticity and high memory effect. However, flat surface material has less modulus of elasticity and high plasticity.

Table 4. Roughness (Ra).

Position	Outer surface roughness values [Ra]
A	3.61
B	3.07
C	3.39
D	3.22
E	3.36
F	4.31
Average	3.49
Std Dev	0.44

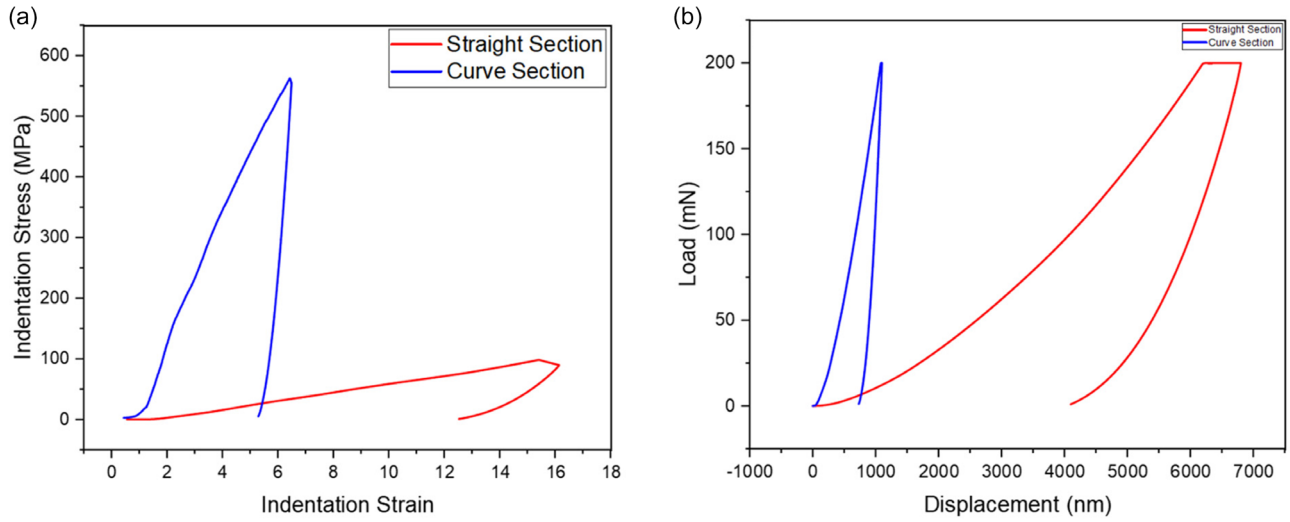

Figure 16. a) Stress–strain curves and b) load displacement curve.

Table 5. Mechanical properties of LMD-fabricated cube sample.[17]

Sample ID	Hardness [HV]	Hardness [MPa]	YS [MPa]	Tensile strength [MPa]
GE as-built	286	2805	469	1066
GE 1200	328	3217	537	1222
GE 1400	325	3187	532	1211

All sample lacked plasticity. This study concluded that a coarse-grained fully lamellar microstructure had low tensile strength which would suggest moderate toughness and ductility at RT.

Comparing Table 4 and 5, it is evident that the pipe, in the as-manufactured state, would perform better than the sample at both room and heat treatment conditions. The true stress–true strain curves of the built pipe are presented in **Figure 17** for the curve and flat (or straight) sections, respectively. Figure 17 shows that the straight curve had limited deformation which was calculated at 1.6% and lacked ductility which meant it failed without any deformation making it brittle, while the curved surface of the pipe built had interesting failure mode wherein it went through a considerable deformation, which was calculated at around 7.4%, and went through plasticity and immediately failed indicating the transition between ductile to brittleness (**Table 6**).

In comparison to the work of[18] Lerch et al. and[19] Baudana et al. the Young's modulus (E) value of the pipe was far lesser than the E value of GE commercial alloy with 168 ± 2 GPa at RT. But the YS and UTS along the curve section were comparably higher than that of GE samples which are 326 and 422 MPa, respectively,[18] indicating that the TiAl pipe curve section would be able to withstand higher stress at RT. However, the TiAl pipe

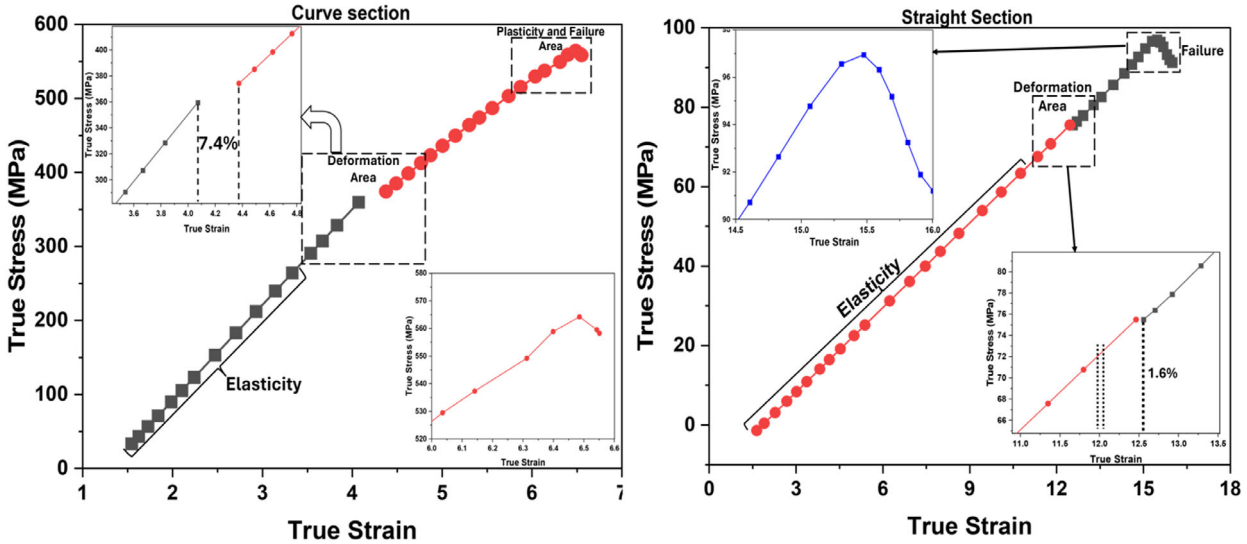

Figure 17. True stress versus true strain curves.

Table 6. Tensile properties of the built pipe.

	Straight section	Curve section
UTS [MPa]	97	564
YS [MPa]	75	360
Young's modulus, E [GPa]	7.1	129
Stiffness, S [N m^{-1}]	0.15525×10^6	0.76227×10^6

along the straight section has drastically very small values of YS and UTS. Consequently, the TiAl alloy pipe demonstrates that it is very brittle along the straight section but shows very good toughness along the curve section. Therefore, the curve section would be able to perform better in terms of deformation under stress than the normal GE alloy. Moreover, it is expected to possess better high-temperature performance and resistance to creep owing to the strengthening mechanism of the heat treatment carried out. It is well acknowledged that ordered intermetallic TiAl-based alloy deforms via a dislocation glide, which can be quite challenging to operate.[20]

Enhancing the tendency for twinning in γ-phase also improves plasticity. The heat treatment may diminish the γ-phase stacking fault energy; thus, this enhancement was be realized but only along the curve section. Furthermore, it has been shown that the lamellar spacing, λ, has a significant impact; for any λ between 4100 nm and the YS, the connection is of the standard Hall–Petch type.[20] Therefore, ductility and work hardening coefficient drop as λ decreases, whereas the YS increases. Depending on whether disordered β or ordered B2 (β_0) is preserved after HT, the existence of B2/β phases along the build direction which aligns with the curve section had a positive effect on RT ductility but was detrimental to the straight section. Once more, even minor alterations to the resulting microstructures have the potential to significantly worsen embrittlement and may not be regarded as a good option for improving mechanical properties overall. The emergence of stronger phases inside the matrix structure and the grain interfaces following heat treatment were identified as the primary causes of the enhanced UTS and YS.

5. Discussions

Lamellar microstructures, of gamma alloys, exhibit high fracture toughness (a property with which material resist fracture) when compared to duplex and equiaxed microstructures.[21] While a duplex microstructures with primary γ-phase and lamellar colonies have some form of RT ductility, fully lamellar microstructures are more brittle.[22,23] On deformation,[22] Bettles et al. reviewed that two-phase and single-phase γ-alloys have multistage deformation mechanisms, whereas single-phase α_2 alloys have a single-stage deformation step. Ti4822 alloy is a γ-phase alloy and would therefore be considered to have multistage deformation steps. To understand failure of the built pipe, the microstructural analyses were recorded for both the flat /outer surface (along the z-direction during printing) and the contour surface. The outer surface was lamellar rich and therefore would exhibit high toughness, and therefore, to investigate the plausible point of failure and failure mechanism in the built pipe, the contour surface was considered. Given that it had impurities and defects (cracks) and the microstructure was lamellar grained with the alpha-rich (aluminum lean) lamellar grain presenting dislocation pile-ups, it was necessary to investigate the failure mode. According to the fracture microstructures, failure would occur but would not be sudden given the elongated dimples that were identified, leading to a conclusion that the failure will be ductile-brittle in nature ("a multistage deformation"). These failure modes were supported by the hardness depression (hardness indents) results. The results showed that the contour surface will undergo no permanent deformation. This means it will have some form of plasticity which according to the deformation area under the curve calculation was determined to be 7.4%. The indentation results were able to prove that the contour surface of the pipe will deform and then go through plasticity before it suddenly fails (brittle failure). The nanoindentation results proved that the contour surface indeed was tough but not as tough as that of the flat surface, and because of the inner roughness value of the pipe, it was extrapolated that the pipe will have moderate pressure drops,[24] leading to the understanding that it will have desired properties to be used as a heat exchanger and will last longer in service.

6. Conclusion and Future Work

The study reports on the theoretical and actual laser direct energy printed 100 mm-long Ti4822 alloy pipe for application as heat exchanger in industries. This work concluded the following: 1) The theoretical and experimental results coincided especially where heat distribution and tapering were of concerns. 2) The microstructure showed that the pipe was lamellar along the z-built direction, indicating good toughness as compared to the contour wherein dislocation pile-ups were observed and results concluded that fracture will occur and the failure will be summarized as ductile-brittle failure. 3) Given the overall toughness of the pipe and the inner surface roughness that correspond to moderate pressure drops, it was concluded that this Ti4822 pipe will have extended use as a heat exchanger, and this will be conducted in future work.

Acknowledgements

The authors would like to acknowledge Council for Scientific and Industrial Research (CSIR), South Africa, and National Research Foundation, South Africa, for funding this research. Also, the authors wish to recognize CSIR and Tshwane University of Technology for making available their world-class research facilities for the undertaking of the research work.

Conflict of Interest

The authors declare no conflict of interest.

Data Availability Statement

The data that support the findings of this study are available from the corresponding author upon reasonable request.

Keywords

COMSOL Multiphysics, fractures, hardness impressions, laser metal deposition, nanoindentation, Ti4822 alloy

Received: March 14, 2025
Revised: October 3, 2025
Published online:

[1] M. Tlotleng, S. Pityana, S. Motha, *Appl. Sci.* **2023**, *13*, 5725.
[2] N. A. Nochovnaya, P. V. Panin, A. S. Kochetkov, K. A. Bokov, *Met. Sci. Heat Treat.* **2014**, *56*, 364.
[3] M. Balichakra, S. Bontha, P. Krishna, V. K. Balla, *Mater. Res. Express* **2019**, *6*, 1.
[4] L. Yan, W. Li, X. Chen, Y. Zhang, J. Newkirk, F. Liou, D. Dietrich, *JOM* **2017**, *69*, 586.
[5] G. A. Farotade, O. S. Adesina, A. Kolesnikov, A. P. I. Popoola, *Mater. Res. Express* **2019**, *6*, 046516.
[6] S. Morville, M. Carin, P. Peyre, M. Gharbi, D. Carron, P. Le Masson, R. Fabbro, *J. Laser App.* **2012**, *24*, 1.
[7] G. Yang, W. Wang, L. Y. Qin, X. L. Wang, *Appl. Mech. Mater.* **2012**, *117*, 1633.
[8] W. C. Oliver, G. M. Pharr, *J. Mater. Res.* **1992**, *7*, 1564.
[9] V. Verma, A. Mandal, A. J. I. J. Shukla, *Int. J. Adv. Res. Innov.* **2017**, *5*, 459.
[10] B. Mallikarjuna, S. Bontha, P. Krishna, V. K. Balla, *J. Mater. Res. Technol.* **2021**, *15*, 6231.
[11] D. Zhang, Z. Feng, C. Wang, Z. Liu, D. Dong, Y. Zhou, R. Wu, *J. Therm. Spray Technol.* **2017**, *26*, 831.
[12] L. Nuñez, C. M. Downey, I. J. van Rooyen, I. Charit, M. R. Maughan, *Int. J. Adv. Manuf. Technol.* **2024**, 1, https://doi.org/10.1007/s00170-024-13587-8.
[13] Y. W. Kim, *Mater. Sci. Eng.: A* **1995**, *192*, 519.
[14] R. Gnanamoorthy, Y. Mutoh, N. Masahashi, Y. Mizuhara, *Metall. Mater. Transac. A* **1995**, *26*, 305.
[15] Y. W. Kim, D. M. Dimiduk, *JOM* **1991**, *43*, 40.
[16] R. Ding, Y. Chiu, M. Chu, S. Paddea, G. Su, *Philos. Mag.* **2020**, *100*, 982.
[17] M. Tlotleng, S. Skhosane, S. Pityana, in *11th Int. Symp. on High-Temperature Metallurgical Processing*, Springer International Publishing **2020**, pp. 123–131.
[18] B. Lerch, S. Draper, M. Pereira, W. Zhuang, in *Proc. of the 2003 TMS Annual Meeting & Exhibition: 3rd Int. Symp. on Gamma Titanium Aluminides*, San Diego, CA, USA **2003**, p. 1.
[19] G. Baudana, S. Biamino, B. Klöden, A. Kirchner, T. Weißgärber, B. Kieback, M. Pavese, D. Ugues, P. Fino, C. Badini, *Intermetallics* **2016**, *73*, 43.
[20] S. Z. Zhang, Y. B. Zhao, C. J. Zhang, J. C. Han, M. J. Sun, M. Xu, *Mater. Sci. Eng.: A* **2017**, *700*, 366.
[21] R. Gnanamoorthy, Y. Mutoh, N. Masahashi, Y. Mizuhara, *Metall. Mater. Transac. A* **1995**, *26A*, 305.
[22] C. J. Bettles, S. Tochon, M. A. Gibson, B. A. Welk, H. L. Fraser, *Mater. Sci. Eng.: A* **2013**, *575*, 152.
[23] B. Mallikarjuna, E. W. Reutzel, *Manufact. Rev.* **2022**, *9*, 27.
[24] G. Dzarma, A. Adeyemi, A. Taj-Liad, *Int. J. Novel Res. Eng. Pharm. Sci.* **2020**, *7*, 1.
[25] S. Y. Sung, Y. J. Kim, *Intermetallics* **2007**, *15*, 468.